

Searching for the QCD Axion with Gravitational Microlensing

Malcolm Fairbairn^{a,*}, David J. E. Marsh^{a,†} and Jérémie Quevillon^{a,‡}

^a *Kings College London, Strand, London, WC2R 2LS, United Kingdom*

The phase transition responsible for axion dark matter production can create large amplitude isocurvature perturbations which collapse into dense objects known as axion miniclusters. We use microlensing data from the EROS survey, and from recent observations with the Subaru Hyper Suprime Cam to place constraints on the minicluster scenario. We compute the microlensing event rate for miniclusters treating them as spatially extended objects with an extended mass function. Using the published bounds on the number of microlensing events we bound the fraction of DM collapsed into miniclusters, f_{MC} . For an axion with temperature dependent mass consistent with the QCD axion we find $f_{\text{MC}} < 0.22(m_a/100\mu\text{eV})^{-0.57}$, which represents the first observational constraint on the minicluster fraction. We forecast that a high-efficiency observation of ten nights with Subaru would be sufficient to constrain $f_{\text{MC}} \lesssim 0.1$ over the entire QCD axion mass range. We make various approximations to derive these constraints and dedicated analyses by the observing teams of EROS and Subaru are necessary to confirm our results. If accurate theoretical predictions for f_{MC} can be made in future then microlensing can be used to exclude, or discover, the QCD axion. Further details of our computations are presented in a companion paper [1].

The QCD axion [2–7] remains one of the most well-motivated and viable candidates for particle dark matter (DM). The axion is a pseudo-Nambu-Goldstone boson of a spontaneously broken global $U(1)$ symmetry, known as a Peccei-Quinn (PQ) symmetry [8]. PQ symmetry breaking occurs when the temperature of the Universe drops below the symmetry breaking scale $T_{\text{PQ}} \sim f_a$. The cosmology of the axion is determined by the cosmic epoch during which symmetry breaking occurs [9, 10]. If the PQ symmetry is broken after smooth cosmic initial conditions are established (by, for example, inflation) then topological defects and large amplitude axion field fluctuations will be present on scales of order the horizon size at symmetry breaking [11–13]. For models of inflation, the observational bound on the cosmic microwave background tensor to scalar ratio of $r_T \leq 0.07$ [14] implies this scenario for symmetry breaking is only possible for $f_a \lesssim 10^{13}$ GeV.

The Kibble mechanism [15] smoothes the axion field on the horizon scale until such a time that the axion mass becomes cosmically relevant: $3H(T_0) \approx m_a(T_0)$, where $H(T)$ is the Hubble rate and we have allowed temperature dependence of the axion mass. At this epoch, the topological defects decay (we consider only the case with domain wall number equal to unity) [16], and the axion field is left with large amplitude isocurvature fluctuations on the horizon scale.

Once cosmological structure begins to grow at matter-radiation equality, the isocurvature perturbations are converted into curvature perturbations, and promptly collapse into dense bound structures of DM known as *axion miniclusters* [11, 17–22]. The characteristic minicluster mass, M_0 , is given by the total mass of DM con-

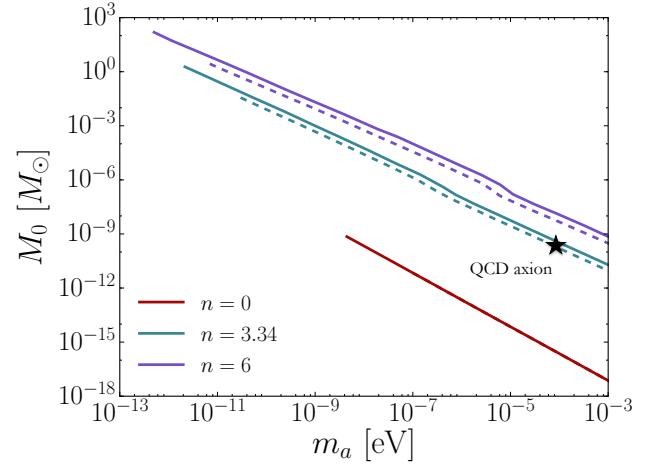


FIG. 1. **The Characteristic Minicluster Mass:** We plot M_0 , as a function of the axion mass, m_a , for different temperature evolutions of the axion mass parameterised by index n . Solid lines show the most realistic assumptions about the relic density, while dashed lines relax those assumptions slightly. When the axion mass is temperature independent ($n = 0$), the two scenarios are equivalent for minicluster mass. Lines terminate at a lower bound on m_a set by the DM relic abundance and the constraint $f_a \lesssim 10^{13}$ GeV for minicluster production.

tained within the horizon at the epoch T_0 :

$$M_0 = \bar{\rho}_a \frac{4}{3} \pi \left(\frac{\pi}{a(T_0)H(T_0)} \right)^3, \quad (1)$$

where a is the cosmic scale factor of the Friedmann-Lemaître-Robertson-Walker metric, and we have considered a spherical patch of radius $R = \pi/k$ for comoving wavevector $k_0 = a(T_0)H(T_0)$ (here and throughout $\hbar = c = 1$).

The temperature T_0 sets the time when the axion field goes from having equation of state $w = -1$ to $w = 0$, and therefore depends on the temperature evolution of the axion mass, $m_a(T) = m_{a,0}(T/T_c)^{-n}$, with $m_a(T < T_c) =$

* malcolm.fairbairn@kcl.ac.uk

† david.marsh@kcl.ac.uk

‡ jeremie.quevillon@kcl.ac.uk

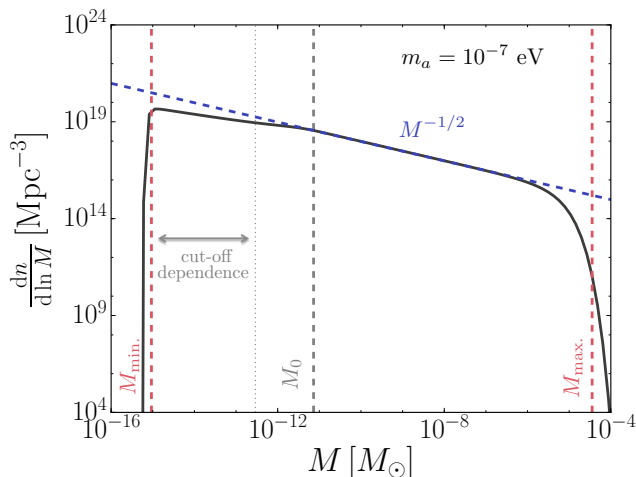


FIG. 2. Parametrization of the Minicluster Mass Function. The mass function can be well fit by two cut-offs and a single slope parameter, $M^{-1/2}$, derived from the white noise initial conditions. For the numerical calculation (solid line), the normalization is fixed to be per unit volume. For the substructure mass function, we normalize by f_{MC} . For illustration we take $m_a = 10^{-7}$ eV and $n = 0$ for the axion mass temperature dependence.

$m_{a,0} \equiv m_a$. The index n parameterizes the sharpness of the phase transition, and the critical temperature $T_c \approx \sqrt{m_a f_a}$ (for the QCD axion $T_c \approx \Lambda_{\text{QCD}} \approx 200$ MeV $\approx 2.5\sqrt{m_a f_a}$; the case $T_c \gg \sqrt{m_a f_a}$ occurs for some axion-like particles [23] and is equivalent to $n = 0$). This phase transition also determines the axion relic density [24–26]. By fixing the relic density such that axions are all of the DM, this determines an n -dependent relationship between m_a and f_a , such that $M_0 = M_0(m_a, n)$.

Following the standard computation for the axion relic density [27], and accounting for uncertainties due to anharmonicity in the axion potential and the decay of topological defects [16], we compute $M_0(m_a)$ for various n (see Fig. 1). As a representative of the QCD axion we take $n \approx 3.34$ from the “interacting instanton liquid” model for the QCD topological susceptibility [27], which is consistent with the results from lattice simulations ($n \approx 3.55 \pm 0.30$ [28, 29]).

We compute the minicluster mass function from hierarchical structure formation following the Press-Schechter [30] approach, as modified in Ref. [31] to account for the axion Jeans scale [32]. Fig. 2 shows the minicluster mass function computed from numerical solution of the linear perturbation equations with white-noise isocurvature initial conditions cut at k_0 . This function is simple to parameterise, as shown in Ref. [1]. The mass function exhibits cut-offs at both a maximum and minimum halo mass. The existence of a minimum mass is consistent with the results of cosmological simulations including the axion de Broglie wavelength and Jeans scale [33, 34], though there is some residual window function and cut-off dependence on small-scales $M < M_0/25$.

The mass function computed from cosmological initial

conditions is normalized per unit volume “in the field”. Since miniclusters collapse much earlier than galactic DM halos, we treat these two periods of gravitational collapse independently, and assume that the minicluster mass function established early on provides the substructure mass function on small-scales. In other words, the minicluster mass function is equivalent to the field mass function within the larger patches that collapse later on into galaxies. We use our parameterized minicluster mass function as the substructure mass function normalized to

$$f_{\text{MC}} = \frac{1}{M_{\text{host}}} \int M \frac{dn}{dM} dM, \quad (2)$$

for host galaxy mass M_{host} and minicluster fraction f_{MC} . The presence of f_{MC} as a free parameter accounts for the fact that, due to the axion population from topological defect decay and the effects of e.g. tidal stripping [35], only a fraction of axions end up bound in miniclusters.

In some cases miniclusters can be massive enough and abundant enough to impact gravitational microlensing. Thus, searches for axion miniclusters are related to searches for non-particle DM candidates such as Massive Compact Halo Objects (MACHOs) [36, 37], and primordial black holes (PBHs, e.g. Refs [38, 39]).

We have computed the gravitational microlensing signal from axion miniclusters for the EROS survey of the Large Magellanic Cloud (LMC) [40] and for recent observations with the Subaru Hyper Suprime Cam (HSC) of Andromeda (M31) [39]. The EROS survey has a high microlensing efficiency for timescales between one day and 1000 days, while HSC observations have high efficiency for timescales between two minutes and seven hours. Thus the two surveys probe different characteristic lens masses [37]. We make various approximations in order to handle the constraints from these surveys in a simple manner, and emphasize that a dedicated analysis by observers is desirable. We compute the lensing signal for miniclusters forming an extended mass distribution, and treat the miniclusters as extended objects.

Microlensing with Miniclusters: A key quantity in gravitational microlensing is the Einstein radius:

$$R_E(x, M) = 2 [GMx(1-x)d_s]^{1/2}, \quad (3)$$

where M is the lens mass, d_s is the distance from the observer to the source, and $x = d/d_s$ where d is the distance from the observer to the lens. For a point-like lens, the Einstein radius defines the shape of the “microlensing tube” [37]. This is the volume within which a lens must pass for the lensing amplification, A , to exceed 1.34, $A = 1.34$ being the threshold applied to the lightcurves in microlensing observations [39, 40].

Although compact, miniclusters are extended objects in terms of microlensing, with the scale radius being far larger than the Einstein radius. We take the characteristic density for a minicluster from the numerical simulations of Kolb & Tkachev [17–20]:

$$\rho_c = 140\delta^3(1+\delta)\rho_a(1+z_{\text{eq}})^3, \quad (4)$$

where ρ_a is the axion density today (assumed to be all the DM), and z_{eq} is the redshift of matter radiation equality (these and the other cosmological parameters we use are determined by the cosmic microwave background anisotropies [41]). The parameter δ is the characteristic overdensity of a minicluster at the time of formation. In numerical simulations miniclusters are observed to have a distribution of values for δ given by $dn/d\delta$ which we take to from the numerical results of Fig. 2 in Ref. [20], and which we fit with a Pearson-VII distribution.

Above the axion de Broglie wavelength (which can be safely neglected in the density profiles for microlensing [1]), we treat the density profiles of miniclusters as Navarro-Frenk-White (NFW) [42] type. Eq. (4) defines the NFW characteristic density $\rho(r) = \rho_c / [(r/r_s)(1 + r/r_s)^2]$, with the scale radius defined from ρ_c after fixing the total mass, M , of the minicluster and assuming the profiles extends to $100 r_s$. An alternative minicluster density profile fixes ρ_c as the core density and the radial dependence as $r^{-9/4}$ from self-similar infall [43]. This will be explored in Ref. [1].

We integrate the three dimensional density profile along the line of sight towards the centre of the halo to obtain a surface density for lensing. We can then calculate the magnification using the expression for an axisymmetric mass distribution with impact parameter ℓ from the line of sight

$$A = [(1 - B)(1 + B - C)]^{-1}, \quad (5)$$

$$C = \frac{1}{\Sigma_c \pi \ell} \frac{dM(\ell)}{d\ell}; \quad B = \frac{M(\ell)}{\Sigma_c \pi \ell^2}; \quad \Sigma_c = \frac{1}{4\pi G d_s x(1-x)}.$$

In this way we compute the shape of the microlensing tube given by the value of ℓ corresponding to a magnification of $A = 1.34$ for a minicluster defined by (M, δ) .

From our numerical lensing calculations, we find that the shape of the microlensing tube is still reasonably well described by $R_E(x, M)$, but with a rescaling factor, \mathcal{R} , that depends on δ and M [1], such that the minicluster microlensing tube is given by:

$$R_{\text{MC}}(x, M, \delta) = \mathcal{R}(\delta, M) R_E(x, M). \quad (6)$$

When a halo of mass M is diffuse, the tube is smaller, $\mathcal{R} \rightarrow 0$; as δ increases and the halo becomes more compact it behaves increasingly like a point mass, $\mathcal{R} \rightarrow 1$.

There is a minimum value of δ below which there is no value of impact parameter ℓ for which $A \geq 1.34$, i.e. $\mathcal{R}(\delta < \delta_{\text{min}}) = 0$ with $\delta_{\text{min.}} = \delta_{\text{min.}}(M)$. This limits the total number of miniclusters that are available as microlensing candidates, and reduces considerably the expected number of microlensing events for miniclusters compared to point masses (MACHOs, PBHs).

The rate of microlensing events of duration \hat{t} for miniclusters is:

$$\frac{d\Gamma}{d\hat{t}} = \frac{32d_s}{\hat{t}^4 v_c^2} \int_0^\infty \left\{ \frac{dn}{d\delta} \int_0^\infty \left[\frac{dn}{dM} \int_0^1 \rho_{\text{DM}} R_{\text{MC}}^4 e^{-Q} dx \right] dM \right\} d\delta \quad (7)$$

where $v_c \approx 220 \text{ km s}^{-1}$ is the local circular speed, ρ_{DM} is the line of sight DM density to the source and we have suppressed the dependencies on, x , M and δ of the integrand. The factor e^{-Q} with $Q = 4R_{\text{MC}}^2/(\hat{t}^2 v_c^2)$ emerges by approximating the Bessel function in the lensing integral [37, 44].

The EROS survey observed the LMC, at a distance $d_{\text{LMC}} = 50 \text{ kpc}$, considering only lensing events of LMC stars by DM in the Milky Way (MW). EROS models the MW as a cored isothermal sphere:

$$\rho_{\text{MW,EROS}}(r) = \rho_0 \frac{R_c^2 + R_\oplus^2}{R_c^2 + r^2}, \quad (8)$$

where $R_\oplus = 8.5 \text{ kpc}$ is the radius of the Earth from the MW centre and the MW halo parameters are $R_c = 5 \text{ kpc}$ and $\rho_0 = 0.0079 M_\odot \text{pc}^{-3}$. A minicluster in the MW at distance d from Earth on the line of sight to the LMC has radial coordinate in the MW halo $r_{\text{MW}}^2(d) = R_\oplus^2 - 2R_\oplus d \cos l_{\text{LMC}} \cos b_{\text{LMC}} + d^2$, where (l, b) are the measured Galactic coordinates.

HSC observed the galaxy of Andromeda (M31). For such an observation, one must consider lensing of stars in M31 by both DM in the MW and in M31 itself. Thus the event rate is given by $d\Gamma = d\Gamma_{\text{MW}} + d\Gamma_{\text{M31}}$ and the DM density is the sum of both halos. HSC model both the MW and M31 as NFW profiles with halo parameters from Ref. [45] quoted in Ref. [39]. M31 is at a distance $d_{\text{M31}} = 770 \text{ kpc}$. A minicluster in the MW at distance d from Earth on the line of sight to M31 has radial coordinate $r_{\text{MW}}(d)^2 = R_\oplus^2 - 2R_\oplus d \cos l_{\text{M31}} \cos b_{\text{M31}} + d^2$, while a minicluster in M31 at a distance d from Earth has radial coordinate in M31 $r_{\text{M31}}(d) \approx d_{\text{M31}} - d$.

The number of expected microlensing events is:

$$N_{\text{exp}} = E \int d\hat{t} \frac{d\Gamma}{d\hat{t}} \epsilon(\hat{t}), \quad (9)$$

where E is the total exposure in star-years and $\epsilon(\hat{t})$ is the microlensing efficiency of the survey. EROS give the microlensing efficiency in Fig. 11 of Ref. [40], which we digitize. We take the exposure from Ref. [40] as $E_{\text{EROS}} = 3.68 \times 10^7 \text{ star-years}$.

HSC use a sophisticated Monte Carlo technique to determine the efficiency in each region of the observing field, and separately for different magnitudes of stars. Reproducing such an analysis is beyond the scope of our work and so we make a series of approximations to get a feel for the possible HSC constraints. We take the total number of stars optimistically as $N_s = 10^9$, with an observation of $t_{\text{obs}} = 7 \text{ hours}$ giving an exposure of $E_{\text{HSC}} = 8 \times 10^5 \text{ star-years}$. We model the efficiency from Fig. 14 of Ref. [39] as a step function with $\epsilon = 0.5$ between the sampling of two minutes and the observing time of seven hours.

Results: We show the expected number of microlensing events in the minicluster scenario as a function of M_0 in Fig. 3 for HSC and EROS with $f_{\text{MC}} = 1$. The number of events in HSC is far larger than for EROS due to the huge volume of matter between Earth and M31 leading

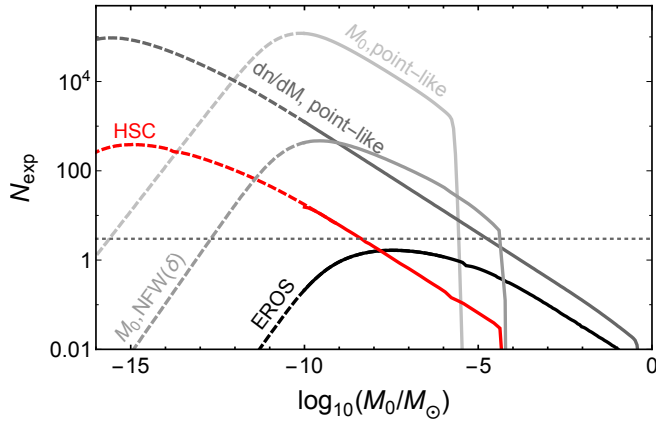


FIG. 3. **Expected Microlensing Events:** The mapping from M_0 to m_a is for $n = 3.34$ (solid lines) and $n = 0$ (dashed lines). The horizontal line shows the 95% C.L. limit. Grey lines show the effects of our modelling of the minicuster mass function and density profile for HSC, with the most realistic case given by the red line. The black lines correspond to the most realistic case for the EROS survey.

to a larger optical depth to microlensing for HSC [39]. To show the effects of our modelling we show four different calculations of N_{exp} for HSC. In the first, we treat miniclusters as point like with a Dirac-delta-function mass distribution at M_0 : this is the least realistic model for miniclusters giving the most events. We then add, individually, our treatments of dn/dM and $dn/d\delta$. The mass function shifts the central value of M_0 that the survey is sensitive to to smaller values due to the spread of miniclusters to M larger than M_0 from hierarchical structure formation. The non-point-like description reduces the number of events by a factor of $\mathcal{O}(10^2)$ due to the requirement of large δ such that $\mathcal{R} > 0$. The combined prescription we adopt is the most conservative, as it gives the weakest constraints on the QCD axion.

Taking both EROS and HSC to have observed zero microlensing candidates the Poisson statistics 95% C.L. limit on the number of expected events is $N_{\text{exp}} \leq 3$ [39, 40]. Using this limit we find the constraints on f_{MC} as a function of axion mass m_a presented in Fig. 4. We find that EROS is unable to place a bound on $f_{\text{MC}} < 1$. HSC places very strong bounds on f_{MC} for an axion-like particle with $n = 0$, reaching as low as $f_{\text{MC}} \approx 8.0 \times 10^{-3}$ for $m_a \approx 50 \mu\text{eV}$.

The shaded band shows the allowed mass for the QCD axion fixed by $m_a = 6.6 \mu\text{eV} (10^{12} \text{ GeV}/f_a)$ [2, 3] and the relic density: $50 \mu\text{eV} \lesssim m_a \lesssim 200 \mu\text{eV}$ [46]. The solid lines represent temperature evolution of the axion mass with $n = 3.34$: where these lines intersect the shaded band, f_{MC} is bounded for the QCD axion, and we find $f_{\text{MC}} < 0.22(m_a/100 \mu\text{eV})^{-0.57}$.

These results could be substantially improved as we show in Fig. 4 (inset) where the blue line shows a hypothetical improved observation by HSC, extending to ten nights with an efficiency $\epsilon \sim 1$, leading to a forecast bound of $f_{\text{MC}} \lesssim 0.1$ for the QCD axion. We advo-

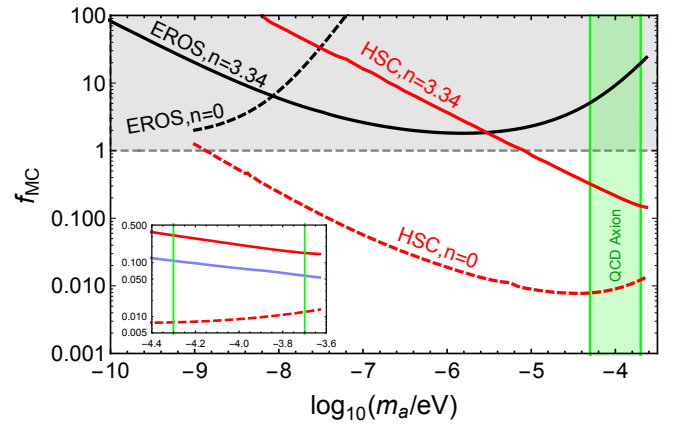


FIG. 4. **Limits on the Fraction of DM collapsed into Miniclusters:** The mapping from M_0 to m_a is for $n = 3.34$ (solid lines) and $n = 0$ (dashed lines). The shaded region shows the allowed mass for the QCD axion in this scenario. Where the solid lines intersect this region, f_{MC} is constrained for the QCD axion. The inset shows a zoom-in on this region. The blue line in the inset shows a hypothetical improved observation by HSC, extending to ten nights with an efficiency $\epsilon \sim 1$.

cate a dedicated analysis of the HSC microlensing data to place more rigorous bounds on f_{MC} than we have approximated, and for a longer microlensing survey in order to improve those bounds further. Additional theoretical modelling of microlensing with miniclusters is presented in Ref. [1], including the necessary light curves. We also discuss various theoretical uncertainties in Ref. [1] that can give small shifts in the constraints. The largest uncertainty comes from our modelling of the lensing efficiency. We are confident, however, that a more thorough analysis by the observing teams will show that HSC, and microlensing in general, is now a powerful tool to constrain the QCD axion.

In this paper we have used microlensing to place the first observational bounds on the DM axion minicuster fraction, f_{MC} . This quantity is poorly understood theoretically, and naively could be order unity. If the minicuster fraction were unity then axion detection in the lab [47] in this mass range, e.g. by “MADMAX” [48], would be much more difficult due to the small probability of an encounter between the Earth and a minicuster. Thus bounding f_{MC} observationally is an important task.

If axions are detected directly in the lab in future then tidal stripping of miniclusters allows f_{MC} to be measured from the phase-space distribution [35, 43]. Independently of the minicuster fraction, axions in the mass range accessible to microlensing can be detected via the force they mediate in the proposed experiment “ARIADNE” [49].

Finally, if accurate theoretical predictions for f_{MC} could be made through numerical simulation, then our results, or future microlensing surveys, could be used to exclude the existence of the QCD axion, or indeed discover evidence for it.

Acknowledgments We acknowledge useful discussions with Anne Green, Edward Hardy, Hitoshi Murayama, and Simon Rozier. MF is funded by the European Research Council under the European Union’s Horizon 2020 program (ERC Grant Agreement no.648680 DARK-

HORIZONS). JQ and MF are supported by the UK STFC Grant ST/L000326/1 while DJEM is supported by a Royal Astronomical Society Postdoctoral Fellowship. DJEM acknowledges hospitality of the Yukawa Institute and the UTQuest workshop, where part of this work was completed.

-
- [1] M. Fairbairn, D. J. E. Marsh, J. Quevillon, and S. Rozier, In Preparation .
 - [2] S. Weinberg, Phys. Rev. Lett.**40**, 223 (1978).
 - [3] F. Wilczek, Phys. Rev. Lett.**40**, 279 (1978).
 - [4] J. E. Kim, Phys. Rev. Lett.**43**, 103 (1979).
 - [5] M. A. Shifman, A. I. Vainshtein, and V. I. Zakharov, Nuclear Physics B **166**, 493 (1980).
 - [6] A. Zhitnitsky, Sov.J . Nucl. Phys. **31**, 260 (1980).
 - [7] M. Dine, W. Fischler, and M. Srednicki, Phys. Lett. B **104**, 199 (1981).
 - [8] R. Peccei and H. R. Quinn, Phys. Rev. Lett.**38**, 1440 (1977).
 - [9] P. Sikivie, Axion Cosmology, in *Axions*, edited by M. Kuster, G. Raffelt, and B. Beltrán, , Lecture Notes in Physics, Berlin Springer Verlag Vol. 741, p. 19, 2008, astro-ph/0610440.
 - [10] D. J. E. Marsh, Phys. Rep.**643**, 1 (2016), 1510.07633.
 - [11] C. J. Hogan and M. J. Rees, Phys. Lett. B **205**, 228 (1988).
 - [12] P. Sikivie, Phys. Rev. Lett.**48**, 1156 (1982).
 - [13] D. Harari and P. Sikivie, Phys. Lett. B **195**, 361 (1987).
 - [14] BICEP2 Collaboration *et al.*, Phys. Rev. Lett.**116**, 031302 (2016), 1510.09217.
 - [15] T. W. B. Kibble, Journal of Physics A Mathematical General **9**, 1387 (1976).
 - [16] M. Kawasaki, K. Saikawa, and T. Sekiguchi, Phys. Rev. D**91**, 065014 (2015), 1412.0789.
 - [17] E. W. Kolb and I. I. Tkachev, Phys. Rev. Lett.**71**, 3051 (1993), hep-ph/9303313.
 - [18] E. W. Kolb and I. I. Tkachev, Phys. Rev. D**49**, 5040 (1994), astro-ph/9311037.
 - [19] E. W. Kolb and I. I. Tkachev, Phys. Rev. D**50**, 769 (1994), astro-ph/9403011.
 - [20] E. W. Kolb and I. I. Tkachev, ApJLett**460**, L25 (1996), astro-ph/9510043.
 - [21] K. M. Zurek, C. J. Hogan, and T. R. Quinn, Phys. Rev. D**75**, 043511 (2007), astro-ph/0607341.
 - [22] E. Hardy, ArXiv e-prints (2016), 1609.00208.
 - [23] A. G. Dias, A. C. B. Machado, C. C. Nishi, A. Ringwald, and P. Vaudrevange, Journal of High Energy Physics **6**, 37 (2014), 1403.5760.
 - [24] J. Preskill, M. B. Wise, and F. Wilczek, Phys. Lett. B **120**, 127 (1983).
 - [25] L. F. Abbott and P. Sikivie, Phys. Lett. B **120**, 133 (1983).
 - [26] M. Dine and W. Fischler, Phys. Lett. B **120**, 137 (1983).
 - [27] O. Wantz and E. Shellard, Phys. Rev. D**82**, 123508 (2010), 0910.1066.
 - [28] S. Borsanyi *et al.*, Physics Letters B **752**, 175 (2016), 1508.06917.
 - [29] S. Borsanyi *et al.*, Nature **539**, 69 (2016), 1606.07494.
 - [30] W. H. Press and P. Schechter, Astrophys. J.**187**, 425 (1974).
 - [31] D. J. E. Marsh and J. Silk, MNRAS**437**, 2652 (2014), 1307.1705.
 - [32] M. Khlopov, B. Malomed, and I. Zeldovich, MNRAS**215**, 575 (1985).
 - [33] H.-Y. Schive, T. Chiueh, and T. Broadhurst, Nature Physics **10**, 496 (2014), 1406.6586.
 - [34] P. S. Corasaniti, S. Agarwal, D. J. E. Marsh, and S. Das, ArXiv e-prints (2016), 1611.05892.
 - [35] P. Tinyakov, I. Tkachev, and K. Zioutas, JCAP**1**, 035 (2016), 1512.02884.
 - [36] B. Paczynski, Astrophys. J.**304**, 1 (1986).
 - [37] K. Griest, Astrophys. J.**366**, 412 (1991).
 - [38] A. M. Green, Phys. Rev. D**94**, 063530 (2016), 1609.01143.
 - [39] H. Niikura *et al.*, ArXiv e-prints (2017), 1701.02151.
 - [40] P. Tisserand *et al.*, A&A**469**, 387 (2007), astro-ph/0607207.
 - [41] Planck Collaboration *et al.*, A&A**594**, A13 (2016), 1502.01589.
 - [42] J. F. Navarro, C. S. Frenk, and S. D. White, Astrophys. J.**490**, 493 (1997), astro-ph/9611107.
 - [43] C. A. J. O’Hare and A. M. Green, ArXiv e-prints (2017), 1701.03118.
 - [44] C. Alcock *et al.*, Astrophys. J.**461**, 84 (1996), astro-ph/9506113.
 - [45] A. Klypin, H. Zhao, and R. S. Somerville, Astrophys. J.**573**, 597 (2002), astro-ph/0110390.
 - [46] G. Ballesteros, J. Redondo, A. Ringwald, and C. Tamarit, ArXiv e-prints (2016), 1610.01639.
 - [47] P. W. Graham, I. G. Irastorza, S. K. Lamoreaux, A. Lindner, and K. A. van Bibber, Annual Review of Nuclear and Particle Science **65**, 485 (2015), 1602.00039.
 - [48] The MADMAX Working Group *et al.*, ArXiv e-prints (2016), 1611.05865.
 - [49] A. Arvanitaki and A. A. Geraci, Phys. Rev. Lett.**113**, 161801 (2014), 1403.1290.